

Electronic Supplementary Information (ESI)

A novel polyoxometalate-based hybrid containing 2D [CoMo₈O₂₆]_∞ structure as anode for lithium-ion batteries

Xiaoxia Chen,^{a, #} Zhi Wang,^{a, #} Ranran Zhang,^a Liqiang Xu^{a, *} and Di Sun^{a, *}

^aSchool of Chemistry and Chemical Engineering, Shandong University, Jinan, 250100, P. R.

China

Email: dsun@sdu.edu.cn, xulq@sdu.edu.cn.

#These authors contributed equally to this work.

Materials and Instruments.

All the reagents and solvents employed were commercially available and used as received without further purification. The elemental analyses (C, H, N contents) were determined on a CE instruments EA 1110 analyzer. Thermogravimetric (TG) curves were measured from 30 to 800 °C on a NETZSCH TG 209 F1 Iris® Thermogravimetric Analyser at the heating rate 10 °C/min under N₂ atmosphere (20 mL/min). The morphologies and distribution of elements of the products were observed through field emission scanning electron microscopy (FESEM; ZEISS SUPRA-55). X-ray photoelectron spectra (XPS) were carried out using a Kratos AXIS Ultra DLD spectrometer with Al K α X-ray source. IR spectra were recorded on a PerkinElmer Spectrum Two in the frequency range of 4000-400 cm⁻¹. The diffuse-reflectance spectra were recorded on a UV/Vis spectrophotometer (Evolution 220, ISA-220 accessory, Thermo Scientific) using a built-in 10 mm silicon photodiode with a 60 mm Spectralon sphere. The variable-temperature magnetic susceptibilities were measured using a Magnetic Property Measurement System (MPMS) and a SQUID-VSM (superconducting quantum interference device-vibrating sample magnetometer) (Quantum Design, USA).

Electrochemical Measurements.

The electrochemical tests of lithium-storage performances were examined by CR2032 coin cells. The electrodes were composed of 60 wt% active materials, 30 wt% super P and 10 wt% carboxymethyl cellulose sodium (CMC). The mixture was milled for at least 30 min with deionized water as solvent to get a slurry and then the slurry was spread on a copper foil. The copper foil was cut into the discs with a diameter of 12 mm after drying in vacuum at 60 °C for overnight to use as working electrodes. The loading of the active material was about 1-2 mg cm⁻². The coin cells were assembled in a glove box (Mikrouna, Super 1220/750/900) under ultrapure argon. Lithium foil was used as reference and counter electrode, a celgard 2300 membrane was used as the separator, and 1 M LiPF₆ in dimethyl carbonate (DMC), diethyl carbonate (DEC), and ethylene carbonate (EC) (volume ratio of 1:1:1) was the electrolyte. The long cycle stability and rate stability of the lithium storage performances were characterized by a Land CT2001A battery cycler in the voltage range of 0.01-3.0 V, and the cyclic voltammetry (CV) curves were performed on electrochemical workstations (CHI 760E). The electrochemical tests of sodium ion storage performances were examined by CR2032 coin cells. The working electrode was prepared by a slurry of 60% active material, 30% Super P and 10% carboxymethyl cellulose sodium (CMC) in deionized water. The preparation method is similar with the anode material for LIBs. The obtained electrode was assembled together with a Na metal foil as the counter electrode, a glass fiber as the separator and 1M NaClO₄ in a mixture of EC-DEC (1:1 volume) with 2% fluoroethylene carbonate (FEC) as the electrolyte in an Ar-filled glovebox.

Synthesis of $\{(H_2bimb)[CoMo_8O_{26}]\}_n$ (1)

A mixture of $(NH_4)_6Mo_7O_{24}\cdot 4H_2O$ (61.8 mg, 0.05 mmol), 1,4-bis(imidazol-1-ylmethyl)benzene (bimb) (11.9 mg, 0.05 mmol) and $Co(NO_3)_2\cdot 6H_2O$ (43.7 mg, 0.15 mmol) and H_2O (6 mL) was adjusted to $pH \approx 3$ with about 1d HCl (6 M) and NaOH (1 M), stirred for 10min at room temperature. The resulting mixture was sealed in a 25-mL Teflon-lined stainless steel autoclave and heated at 180 °C for 3000 mins, after which, it was cooled over 13 h to room temperature. The product was obtained as dark red block-shaped crystals in 40% yield (based on cobalt). Anal. Calc. (found) for $C_{14}H_{16}CoMo_8N_4O_{26}$: C, 11.34 (11.10); H, 1.09 (1.58); N, 3.78 (3.86) %. IR (KBr): $\nu(cm^{-1}) = 3193$ (w), 1572 (m), 1535 (m), 1440 (m), 1388 (w), 1265 (w), 1148 (w), 1082 (m), 965 (s) 887 (s), 712 (s), 551(s), 503 (s).

X-ray Crystallography

Single crystal of the complex **1** with appropriate dimensions was chosen under an optical microscope and quickly coated with high vacuum grease (Dow Corning Corporation) before being mounted on a glass fiber for data collection. Data for them were collected on a Bruker Apex II CCD diffractometer with graphite-monochromated Mo K α radiation source ($\lambda = 0.71073 \text{ \AA}$). Cell parameters were retrieved using SMART software and refined with SAINT on all observed reflections¹. Data reduction was performed with the SAINT software and corrected for Lorentz and polarization effects. Absorption corrections were applied with the program SADABS.¹ All structures were solved by direct methods using SHELXS-97² and refined on F^2 by full-matrix least-squares procedures with SHELXL-97³. Hydrogen atoms were placed in calculated positions and included as riding atoms with isotropic displacement parameters 1.2-1.5 times U_{eq} of the attached C and N atoms.

Table S1 Crystal data for 1

Empirical formula	C ₁₄ H ₁₆ CoMo ₈ N ₄ O ₂₆
Formula weight	1482.76
Temperature/K	298(2)
Crystal system	monoclinic
Space group	C2/c
a/Å	25.443(4)
b/Å	8.2809(12)
c/Å	16.263(2)
α/°	90.00
β/°	113.429(4)
γ/°	90.00
Volume/Å ³	3143.9(8)
Z	4
ρ _{calc} /mg/mm ³	3.133
m/mm ⁻¹	3.703
F(000)	2796.0
Crystal size/mm ³	0.20 × 0.15 × 0.15
2θ range for data collection	5.18 to 50°
Index ranges	-30 ≤ h ≤ 26, -9 ≤ k ≤ 8, -16 ≤ l ≤ 19
Reflections collected	7432
Independent reflections	2756[R(int) = 0.0275]
Data/restraints/parameters	2756/0/240
Goodness-of-fit on F ²	1.061
Final R indexes [I>=2σ (I)]	R ₁ = 0.0202, wR ₂ = 0.0464
Final R indexes [all data]	R ₁ = 0.0240, wR ₂ = 0.0484
Largest diff. peak/hole / e Å ⁻³	0.58/-0.61

Table S2 Selected bond lengths (Å) and angles (°) for 1.

Mo1—O3 ⁱ	2.173 (2)	Mo3—O5	1.696 (2)
Mo1—O9	1.727 (2)	Mo3—O6	1.930 (2)
Mo1—O10	2.028 (2)	Mo3—O12 ⁱ	2.240 (2)
Mo1—O11	1.694 (2)	Mo4—O1	1.685 (2)
Mo1—O13 ⁱⁱ	2.235 (2)	Mo4—O2	1.726 (2)
Mo1—O13	1.909 (2)	Mo4—O3 ⁱ	2.156 (2)
Mo2—O6	1.879 (2)	Mo4—O10	1.941 (2)
Mo2—O7	1.731 (2)	Mo4—O12 ⁱ	2.475 (2)
Mo2—O8	1.688 (2)	Mo4—O12	1.940 (2)
Mo2—O10	2.319 (2)	Co1—O4	2.034 (2)
Mo2—O12 ⁱ	2.195 (2)	Co1—O4 ⁱⁱⁱ	2.034 (2)
Mo2—O13 ⁱⁱ	2.031 (2)	Co1—O7 ^{iv}	2.063 (2)
Mo3—O2	2.363 (2)	Co1—O7 ^v	2.063 (2)
Mo3—O3	1.915 (2)	Co1—O9 ^{iv}	2.111 (2)
Mo3—O4	1.728 (2)	Co1—O9 ^v	2.111 (2)
O3 ⁱ —Mo1—O13 ⁱⁱ	79.47 (8)	O5—Mo3—O3	98.95 (10)
O9—Mo1—O3 ⁱ	159.50 (9)	O5—Mo3—O4	104.14 (11)
O9—Mo1—O10	88.36 (9)	O5—Mo3—O6	97.26 (10)
O9—Mo1—O13 ⁱⁱ	90.13 (9)	O5—Mo3—O12 ⁱ	101.67 (10)
O9—Mo1—O13	102.11 (9)	O6—Mo3—O2	79.07 (9)
O10—Mo1—O3 ⁱ	71.86 (8)	O6—Mo3—O12 ⁱ	72.59 (8)
O10—Mo1—O13 ⁱⁱ	73.91 (8)	O12 ⁱ —Mo3—O2	70.70 (8)
O11—Mo1—O3 ⁱ	88.48 (9)	O1—Mo4—O2	105.88 (11)
O11—Mo1—O9	102.81 (11)	O1—Mo4—O3 ⁱ	98.54 (10)
O11—Mo1—O10	107.01 (10)	O1—Mo4—O10	102.37 (10)
O11—Mo1—O13	101.47 (10)	O1—Mo4—O12 ⁱ	177.06 (9)
O11—Mo1—O13 ⁱⁱ	167.02 (9)	O1—Mo4—O12	104.04 (10)
O13—Mo1—O3 ⁱ	92.13 (8)	O2—Mo4—O3 ⁱ	155.56 (10)
O13—Mo1—O10	146.61 (9)	O2—Mo4—O10	99.64 (10)
O13—Mo1—O13 ⁱⁱ	74.44 (9)	O2—Mo4—O12 ⁱ	76.45 (9)
O6—Mo2—O10	87.30 (9)	O2—Mo4—O12	99.78 (9)
O6—Mo2—O12 ⁱ	74.57 (9)	O3 ⁱ —Mo4—O12 ⁱ	79.11 (8)
O6—Mo2—O13 ⁱⁱ	155.13 (9)	O10—Mo4—O3 ⁱ	73.87 (8)
O7—Mo2—O6	98.10 (10)	O10—Mo4—O12 ⁱ	75.34 (8)
O7—Mo2—O10	87.18 (9)	O12—Mo4—O3 ⁱ	74.60 (8)
O7—Mo2—O12 ⁱ	160.34 (10)	O12—Mo4—O10	141.27 (9)
O7—Mo2—O13 ⁱⁱ	94.63 (9)	O12—Mo4—O12 ⁱ	77.12 (9)
O8—Mo2—O6	102.97 (10)	O4 ⁱⁱⁱ —Co1—O4	99.14 (13)
O8—Mo2—O7	105.44 (11)	O4—Co1—O7 ^{iv}	177.61 (9)
O8—Mo2—O10	162.16 (10)	O4 ⁱⁱⁱ —Co1—O7 ^{iv}	83.01 (9)
O8—Mo2—O12 ⁱ	94.06 (10)	O4 ⁱⁱⁱ —Co1—O7 ^v	177.61 (9)
O8—Mo2—O13 ⁱⁱ	94.03 (10)	O4—Co1—O7 ^v	83.01 (9)
O12 ⁱ —Mo2—O10	74.42 (8)	O4 ⁱⁱⁱ —Co1—O9 ^{iv}	93.34 (9)

O13 ⁱⁱ —Mo2—O10	72.04 (8)	O4—Co1—O9 ^{iv}	90.80 (9)
O13 ⁱⁱ —Mo2—O12 ⁱ	86.37 (8)	O4—Co1—O9 ^v	93.34 (9)
O3—Mo3—O2	80.67 (8)	O4 ⁱⁱⁱ —Co1—O9 ^v	90.80 (9)
O3—Mo3—O6	144.29 (9)	O7 ^v —Co1—O7 ^{iv}	94.85 (13)
O3—Mo3—O12 ⁱ	73.08 (8)	O7 ^v —Co1—O9 ^{iv}	87.65 (9)
O4—Mo3—O2	83.48 (10)	O7 ^{iv} —Co1—O9 ^{iv}	88.03 (9)
O4—Mo3—O3	103.40 (10)	O7 ^{iv} —Co1—O9 ^v	87.65 (9)
O4—Mo3—O6	103.14 (10)	O7 ^v —Co1—O9 ^v	88.03 (9)
O4—Mo3—O12 ⁱ	154.18 (10)	O9 ^v —Co1—O9 ^{iv}	173.61 (11)
O5—Mo3—O2	172.19 (9)		

Symmetry codes: (i) $-x+1, -y+2, -z+1$; (ii) $-x+1, -y+1, -z+1$; (iii) $-x+1, y, -z+3/2$; (iv) $-x+1, y+1, -z+3/2$; (v) $x, y+1, z$.

Fig. S1. The EDS for 1.

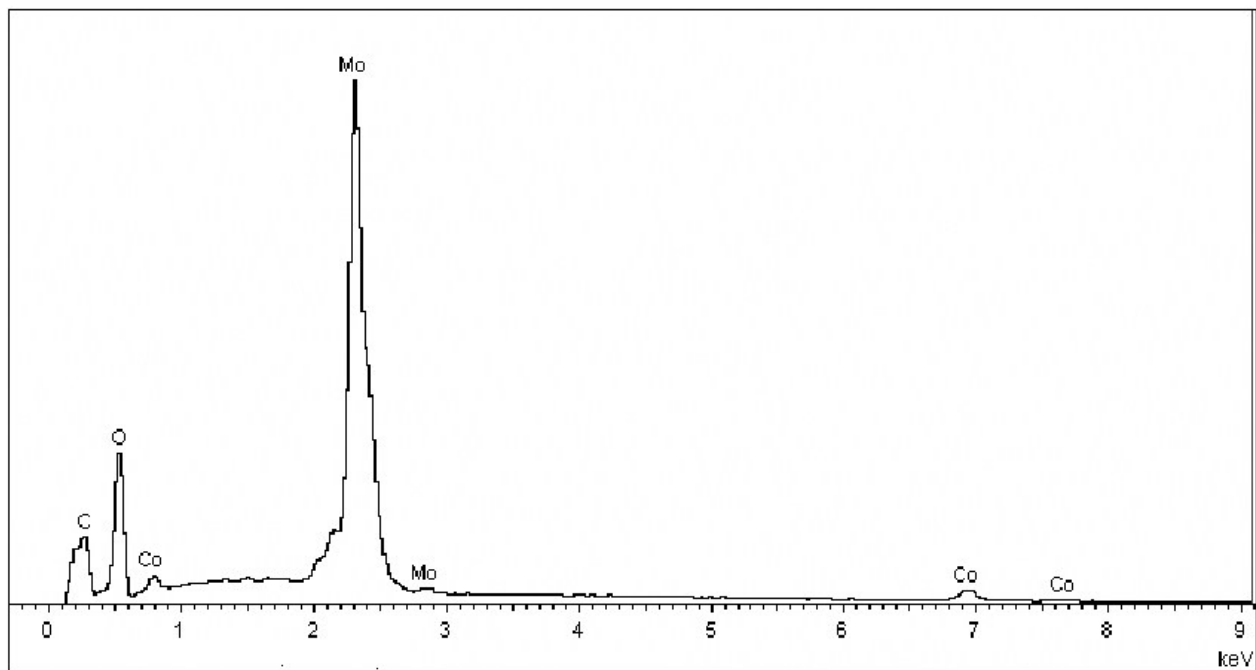


Fig. S2. TGA of 1

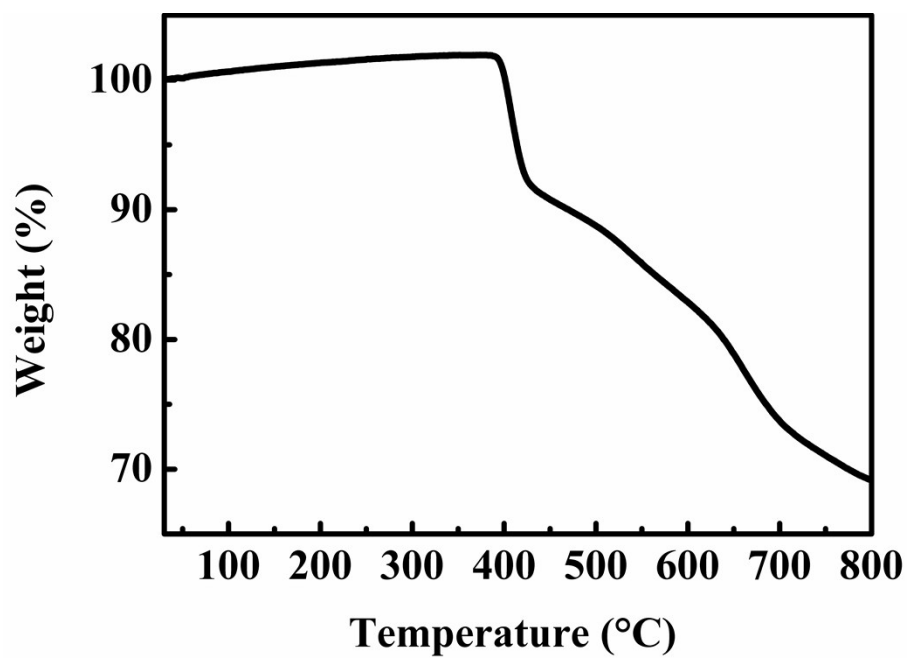


Fig. S3. (a-d) the gradually enlarged SEM images to reveal the details of the crystalline 1, (e) An SEM image of the 1 hybrid material, and the corresponding EDS mapping of (f) carbon, (g) oxygen, (h) cobalt, (i) molybdenum suggesting the homogeneous dispersion of C, O, Co and Mo in the composites.

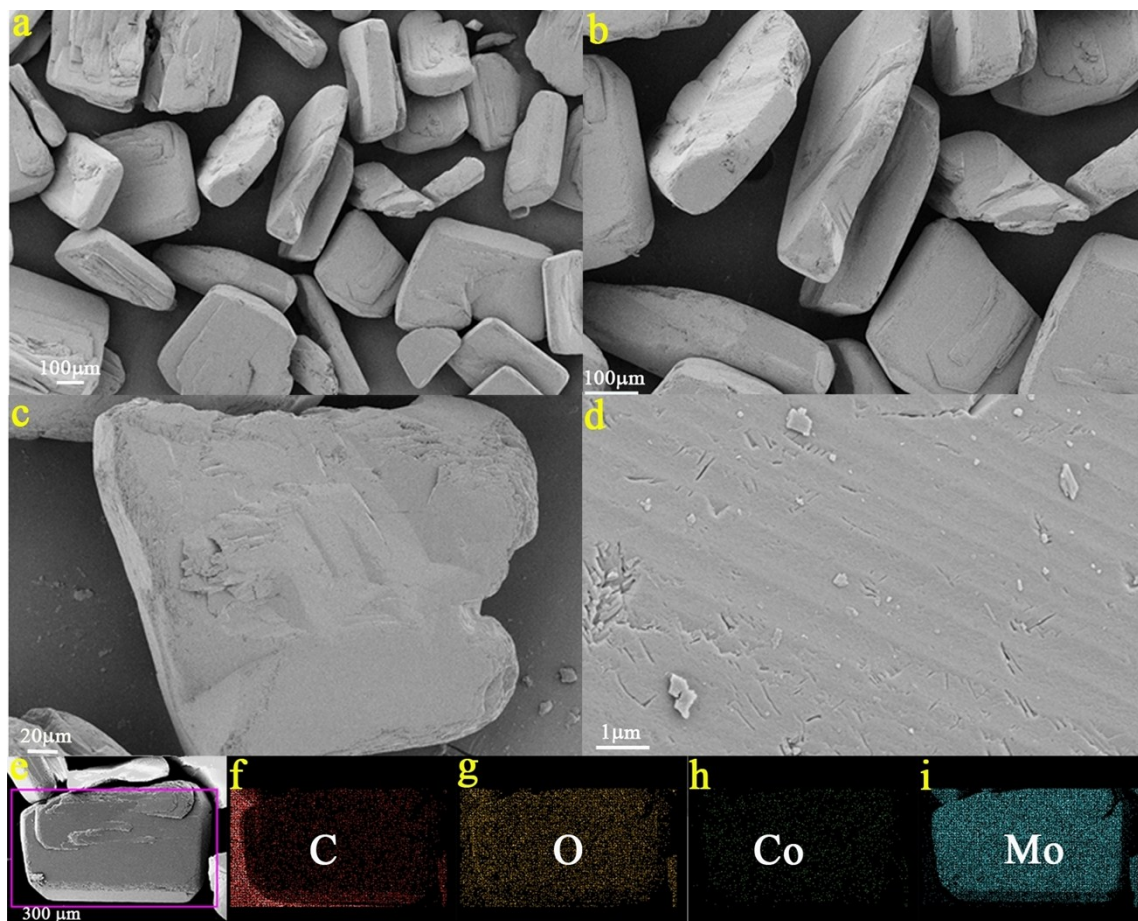
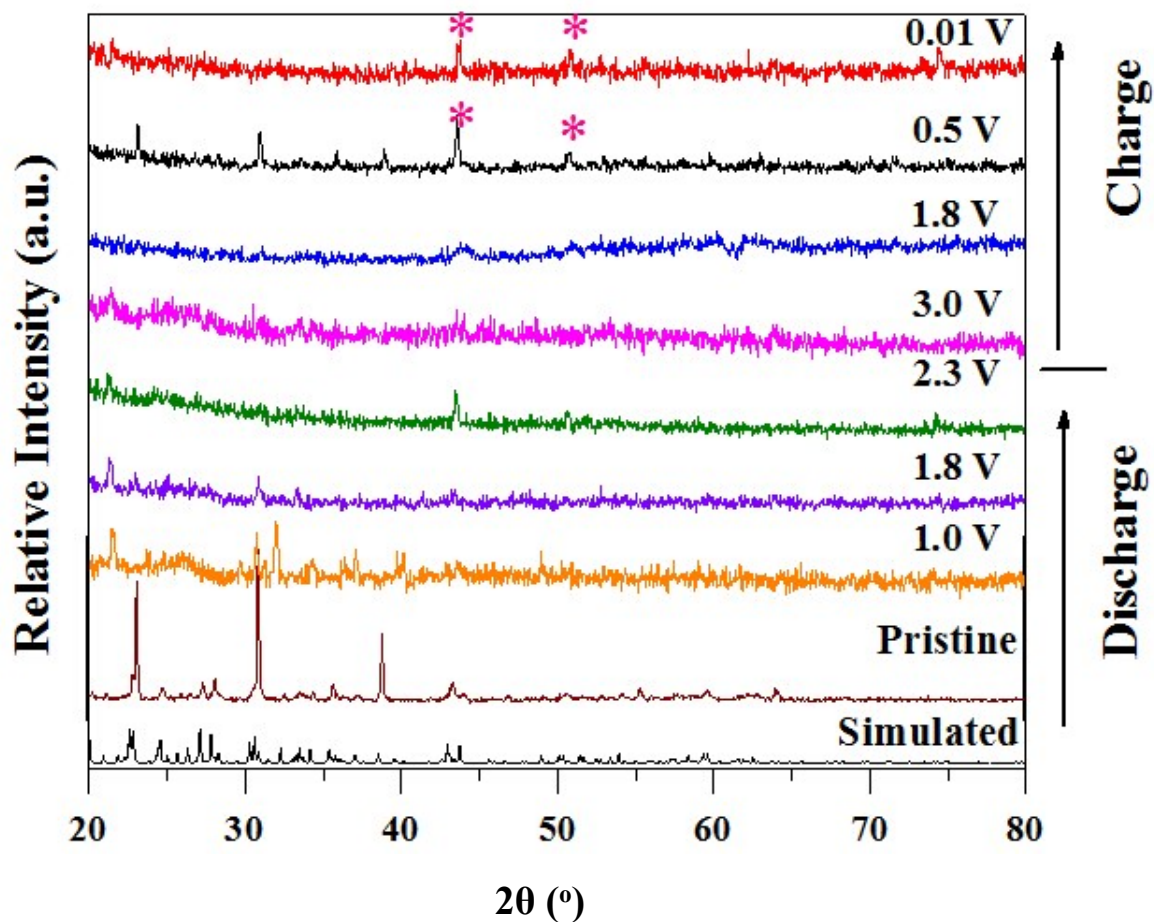


Fig. S4. Ex-situ XRD patterns of **1** collected during the initial charging and discharging at different voltages.



The curves at the bottom are the simulated (black) and experimental (brown) PXRD patterns of **1**, and others are the PXRD patterns of **1** after charging under different voltages ranging from 1.0 to 3.0 V and discharging under different voltages ranging from 1.8 to 0.01 V. The characteristic peaks located at 43.7 and 50.9° are assigned to the (111) and (200) plane of metal Cobalt (JCPDS card no. 15-0806). Any obvious new peak is not found upon discharging to 1.8 V.

Electrochemical mechanism study

As the prepared **1** as anode for LIBs displays excellent long cycle stability, it is interesting to investigate its electrochemical mechanism during cycling. Fig. S4 presents their corresponding ex-situ XRD patterns obtained after first cycle under different voltages. The electrode is discharged under different voltages ranging from 1.8 to 0.01 V, and the marked diffraction peaks ascribed to Co(0) (suggesting the formation of metal cobalt) appear at 0.5 V and their diffraction intensity gradually increase till 0.01 V. Upon charging process, the diffraction intensities of these peaks decrease little by little and vanished at the end of charge. However, no obvious peaks belong to molybdenum appeared during the whole process. The above results are consistent with those of the CV curves. Besides the XRD patterns, the X-ray photoelectron spectroscopy (XPS) analyses are carried out to further detect the metal valences on the surface of the electrode materials before and after cycled for 100 cycles. The XPS survey spectrum (Fig. S5a and 5b) show the presence of Co, O and Mo, along with C elements. As shown in Fig. S5c, the high-resolution Co 2p XPS spectrum of the **1** can be deconvoluted into five different signals with binding energies of 781.1 and 782.88 eV which can be indexed to Co 2p_{3/2} of Co²⁺, while 797.6 eV can be indexed to Co 2p_{3/2} of Co²⁺.⁴ And the satellite peaks appeared at 803.5 and 787.8 eV can be assigned to the shake-up lines of Co²⁺. After 100 cycles, we disassemble the cell and take out of electrode to test the metal valence changes during this process. The high resolution Co 2p XPS spectra (Fig. S5d) can be fitted with five peaks centered at 781.3, 786.54, 797, 802 and 778.5 eV. The binding energies at 781.3 and 797 eV can be assigned to Co 2p_{3/2} and Co 2p_{1/2} of Co²⁺, the binding energies at 778.5 eV can be assigned to Co 2p_{3/2} of Co(0), while the others is attributed to the shake-up lines of Co²⁺. In view of the true that Co can be oxidized easily at room temperature,⁵ we only can detect the weak signal of metal cobalt. According to the high-resolution XPS of Mo, it can be deconvoluted into two signals with binding energies at 235.8 and 232.7 eV before cell cycled in Fig. S5e, which can be indexed to Mo 3d_{3/2} and Mo 3d_{5/2} of Mo⁶⁺.⁶ When cell cycled 100 cycles later, the binding energies (Fig. S5f) at 232.66 and 230.709 eV can be assigned to Mo 3d_{5/2} of Mo⁶⁺, the other two can be attributed to Mo 3d_{3/2} of Mo⁶⁺. These results are consistent with the description of the CV curves and ex-situ XRD results.

Fig. S5. The wide angle XPS survey spectrum (a, b) high-resolution Co 2p in 1 before and after cell cycling (c, d) and high-resolution Mo 3d in 1 before and after cell cycling (e, f).

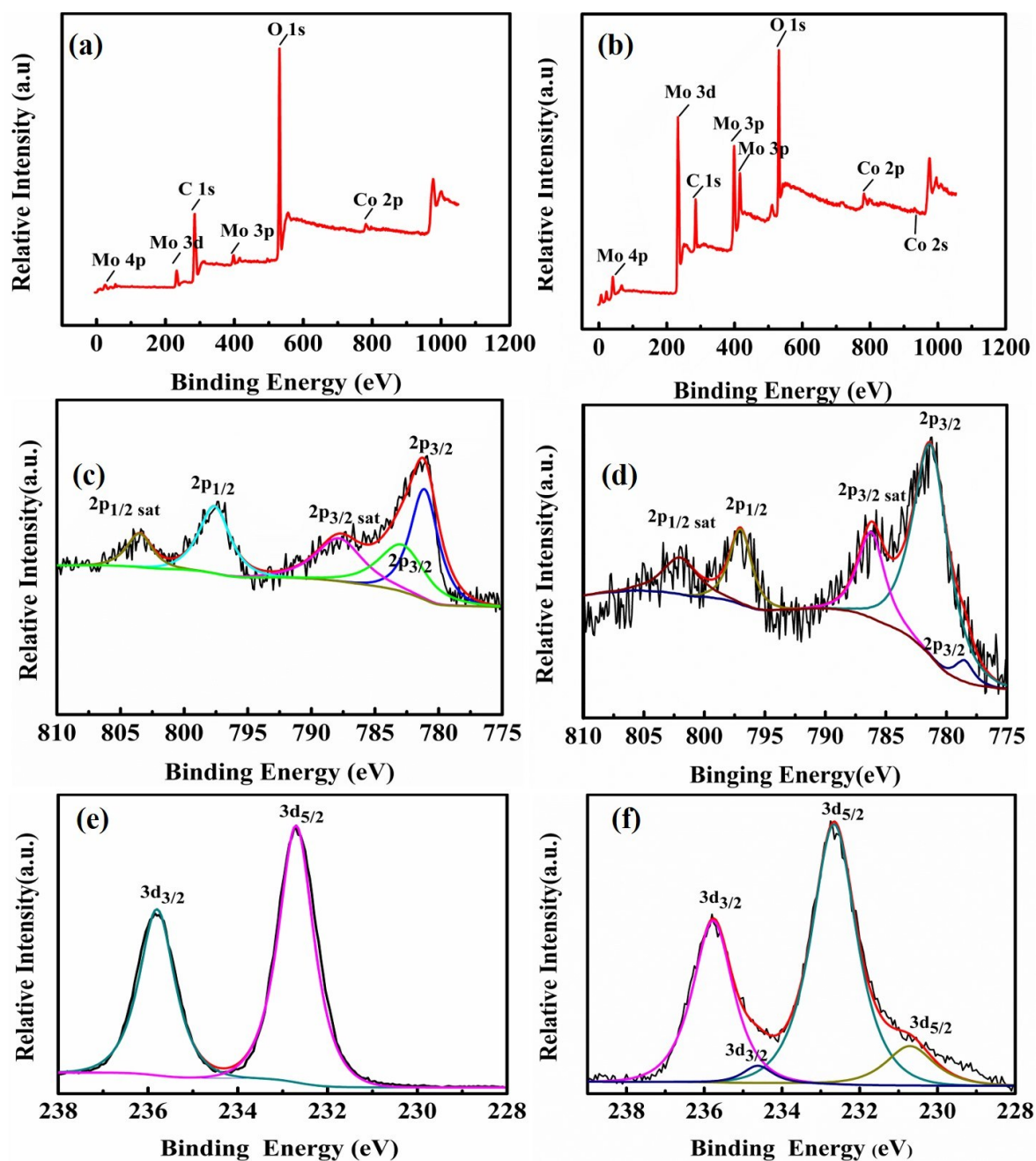
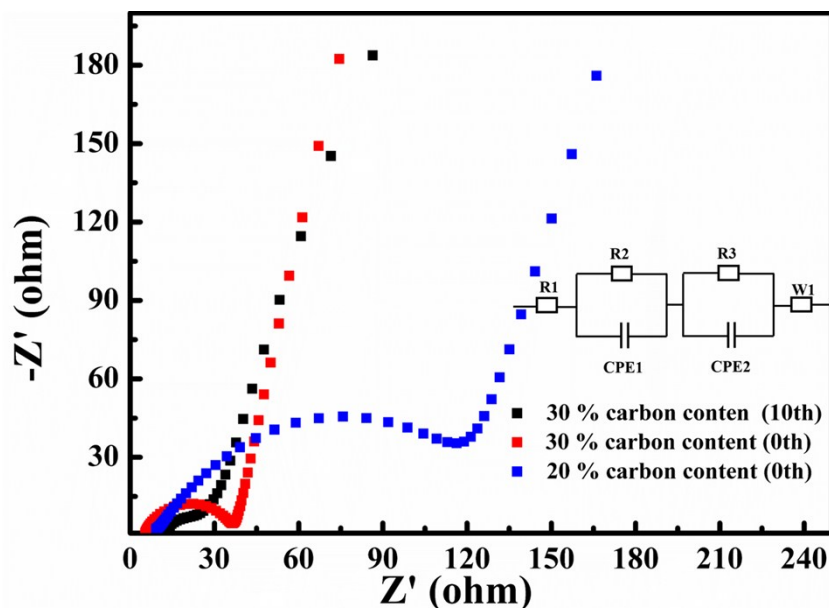


Fig. S6. The Nyquist plots of the impedance spectra of the 1 electrode. Inset: the equivalent circuit model.



To demonstrate the origin behind the high electrochemical performance of prepared material, we have measured the electrochemical impedance spectroscopy (EIS) of **1** between 100 kHz and 0.1 Hz at open-circuit voltage (~ 3 V) vs Li/Li⁺. As shown in Fig. S6, the Nyquist plots of the electrodes consist of low-frequency line and a high-frequency semicircle. The diameter of the semicircle is associated with the charge transfer resistance (R_{ct}),⁹⁻¹⁰ and a slope straight line in the low frequency region represents Warburg impedance of lithium ion diffusion. Fig. S6 displays the Nyquist plots of the initial and after circulation of **1** electrode at room temperature. After 10 cycles, the **1** electrode shows smaller semicircle than the fresh electrode which contain different carbon content before cycle. The decreased R_{ct} value (28.2 Ω) of **1** electrode after cycling may be attributed to the activation of electrode materials and the full infiltration of electrolyte into electrode materials. Compared to other reported POMs material,¹¹⁻¹⁴ the R_{ct} value of **1** electrode contain 30 wt% carbon is even smaller than some high conducting polymer coated hybrid, such as polyoxometalate/polyaniline synthesized through interfacial polymerization method (the R_{ct} value of PANI/PMo₁₂ is 93.6 Ω).¹¹ The lower resistance of **1** electrode than those of other reported POMs material is believed to be helpful for enhanced electrochemical performance.¹⁴

1 as anode material for sodium ion batteries (SIBs)

Take account of the large layer spacing into consideration, the as-obtained **1** may suitable for sodium ion insertion and desorption when used as anode for SIBs.⁷ The electrochemical cycling stability of the **1** as anode for SIBs is evaluated by galvanostatic discharge–charge measurements at a current density of 50 mA g⁻¹ in the potential range from 0.01 to 3 V. As shown in Fig. S7a, the initial discharge capacity of the electrode is 585 mA h g⁻¹, and 81.6 mA h g⁻¹ is remained after 500 cycles. Fig. S7b shows the galvanostatic charge-discharge profiles at a current density of 50 mA g⁻¹. The initially capacity is 585 mA h g⁻¹. The galvanostatic cycling performance obtained at various current rates of **1** are presented in Fig. S7c. The results show that the Co-doped POMs exhibit excellent rate capabilities, when the current is increased from 150 to 450 mA g⁻¹, the discharge capacity decreased slowly from 135 to 72 mA h g⁻¹, respectively. The gap of capacity between 150 and 450 mA g⁻¹ is very little.

Fig. S7. Cycle performance and coulombic efficiency of 1 as anode for SIBs. (b) Galvanostatic discharge and charge profiles of the 1 at 50 mA g⁻¹ (c) Rate capability at different current densities.

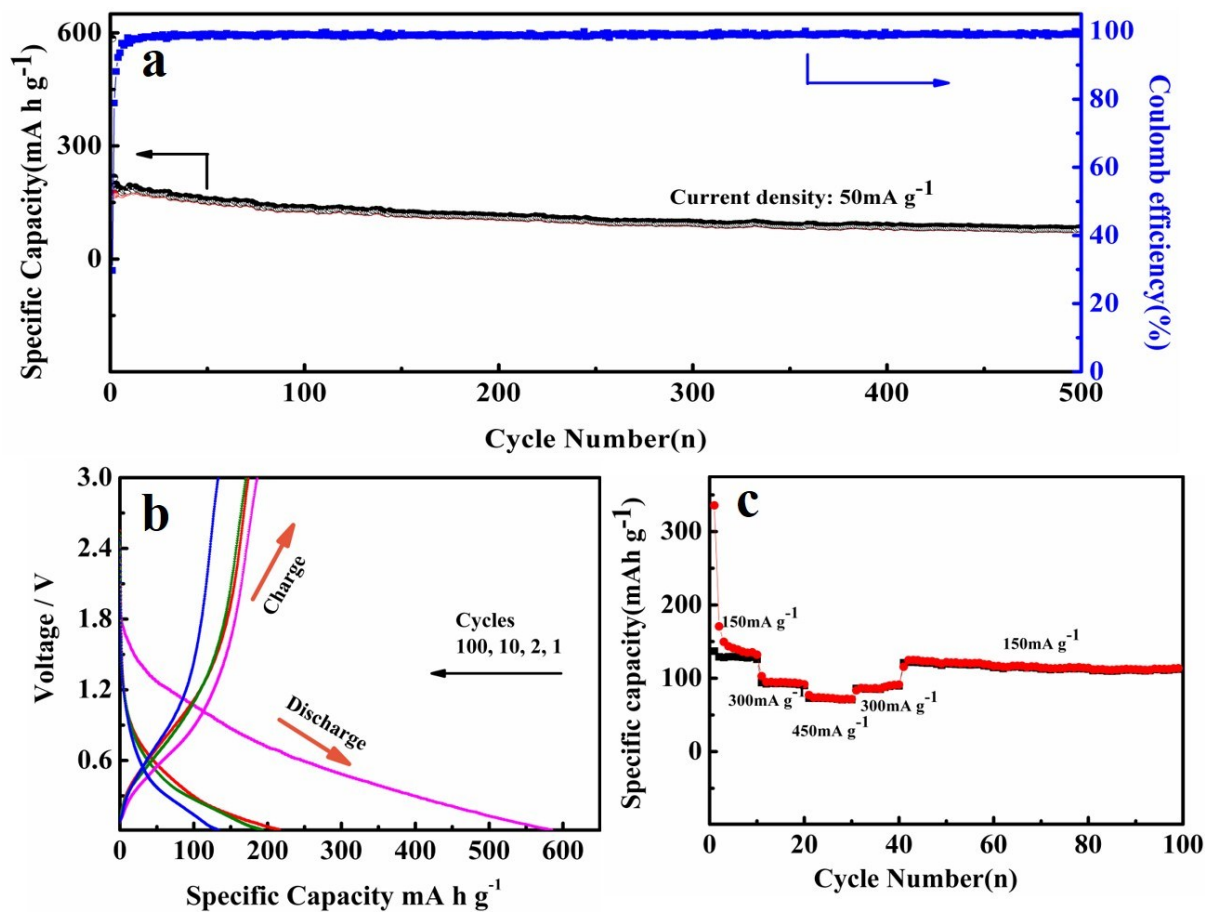
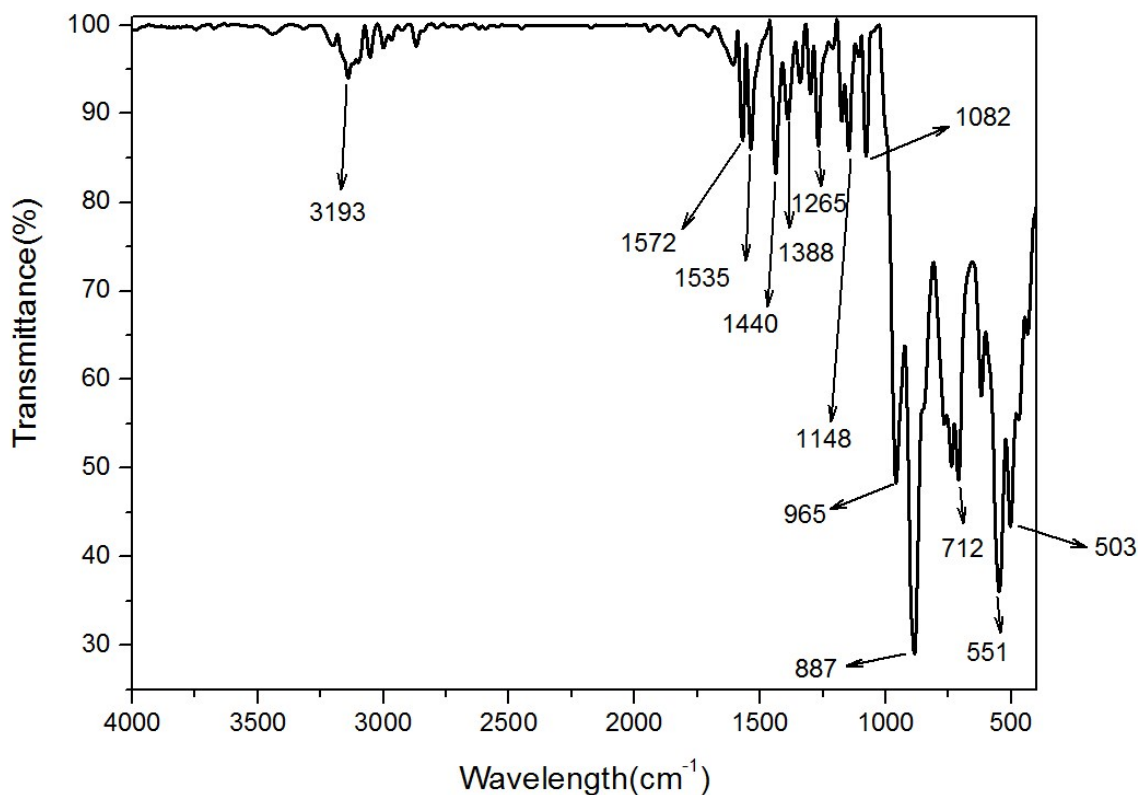
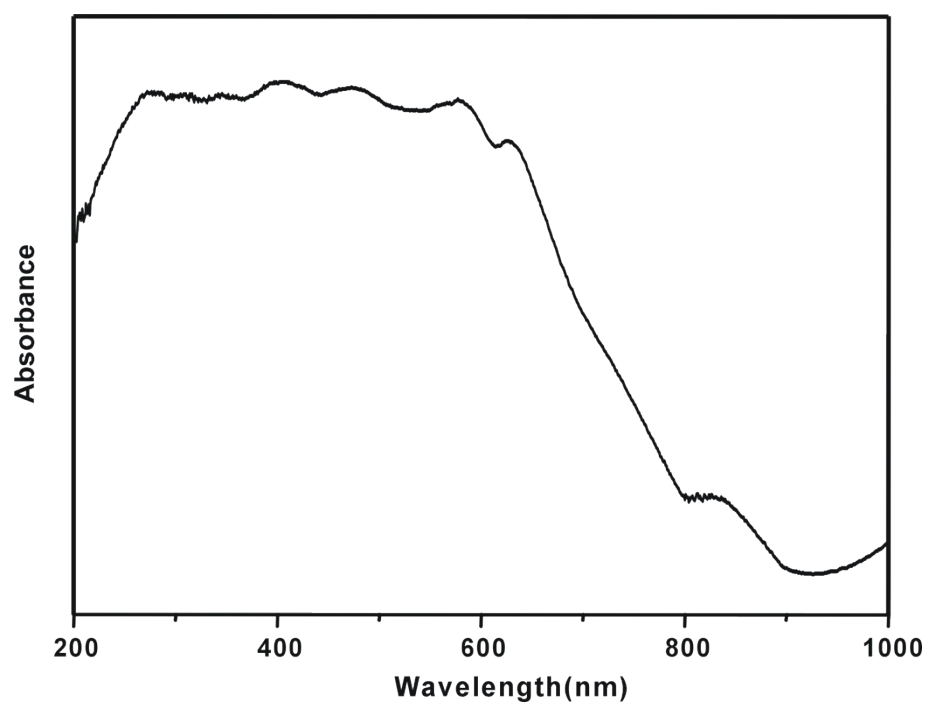


Fig. S8. IR spectrum of **1**



The IR spectrum of compound **1** was recorded between 400 and 4000 cm⁻¹ with KBr pellet. The strong peaks at 965, 887, 712 cm⁻¹ are ascribed to the characteristic vibration peaks of $\nu_{\text{as}}(\text{Mo}-\text{O}_{\mu 1})$, $\nu_{\text{as}}(\text{Mo}-\text{O}_{\mu 2}-\text{Mo})$ and $\nu_{\text{as}}(\text{Mo}-\text{O}_{\mu 3}-\text{Mo})$, respectively.⁸ The peaks at 1572-1440 cm⁻¹ are indicative of $\nu(\text{C}-\text{N})$ vibrations of 1,4-bis(imidazol-1-ylmethyl) benzene ligand. Furthermore, the broad peak near to 3200 cm⁻¹ can be assigned to $\nu(\text{N}-\text{H})$ of the protonated 1,4-bis(imidazol-1-ylmethyl) benzene ligand.

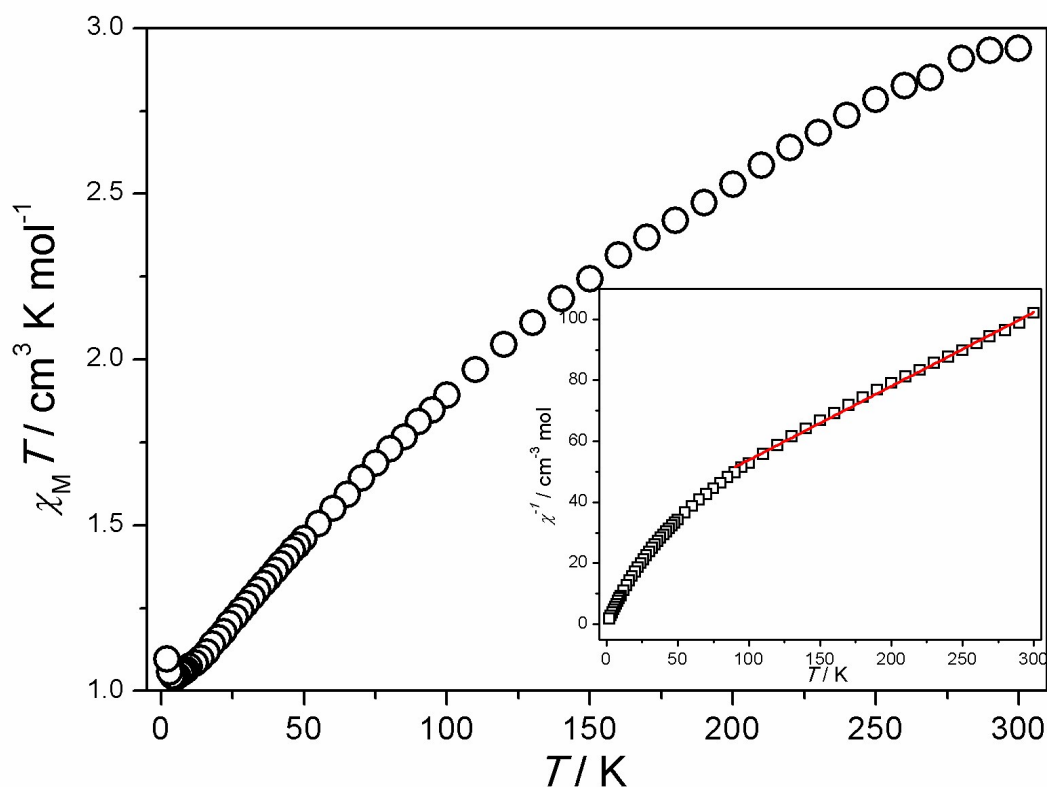
Fig. S9. The UV-Vis spectrum of 1



Magnetism behavior of **1**.

The variable-temperature magnetic measurement of **1** was performed in the temperature range of 2–300 K under an applied magnetic field of 1 kOe (Fig. S10). The experimental $\chi_M T$ value of **1** at room temperature is $2.94 \text{ cm}^3 \text{ mol}^{-1} \text{ K}$, which is slightly higher than the spin-only value $1.875 \text{ cm}^3 \text{ mol}^{-1} \text{ K}$ for mononuclear Co(II) ion ($g = 2$, $s = 3/2$), ascribing to the contribution of Co(II) ions. Upon cooling from room temperature, the $\chi_M T$ value decreases smoothly and then reaches to a minimum of $1.04 \text{ cm}^3 \text{ mol}^{-1} \text{ K}$ at 5.0 K, it increases to $1.09 \text{ cm}^3 \text{ mol}^{-1} \text{ K}$ at 2.0 K. A fit of the χ_M^{-1} above 100 K to the Curie–Weiss law gives a Curie constant $C = 4.20 \text{ cm}^3 \text{ mol}^{-1} \text{ K}$ and a Weiss temperature $\theta = -120.50 \text{ K}$. The negative value of the Weiss temperature further indicates the presence of antiferromagnetic interactions.

Fig. S10. Experimental magnetic data plotted as $\chi_M T$ versus T for **1**. The inset showing $1/\chi$ versus T for **1**.



Supplementary References:

1. Bruker. *SMART, SAINT and SADABS*. Bruker AXS Inc. Madison, Wisconsin, USA, 1998.
2. G. M. Sheldrick, *SHELXS-97*, Program for X-ray Crystal Structure Determination, University of Gottingen, Germany.
3. G. M. Sheldrick, *SHELXL-97*, Program for X-ray Crystal Structure Refinement, University of Gottingen, Germany, 1997.
4. S. Zhu, J. Li, X. Deng, C. He, E. Liu, F. He, C. Shi and N. Zhao, *Adv. Funct. Mater.*, 2017, **27**, 1605017.
5. M. E. Bridge and R. M. Lambert, *Surface Science*, 1979, **82**, 413.
6. Z. Zhang, H. Yoshikawa, Z. Zhang, T. Murayama, M. Sadakane, Y. Inoue, W. Ueda, K. Awaga and M. Hara, *Eur. J. Inorg. Chem.*, 2016, **2016**, 1242.
7. X. Xiang, X. Li, K. Chen, Y. Tang, M. Wan, X. Ding, L. Xue, W. Zhang and Y. Huang, *J. Mater. Chem. A*, 2016, **4**, 18084.
8. (a) C. Rocchiccioli-Deltcheff, M. Fournier, R. Franck and R. Thouvenot, *Inorg. Chem.*, 1983, **22**, 207; (b) W. G. Klemperer and W. Shum, *J. Am. Chem. Soc.*, 1976, **98**, 8291.
9. (a) J. Xie, Y. Zhang, Y. Han and C. Li, *ACS Nano*, 2016, **10**, 5304; (b) C. F. Dong and L.

- Q. Xu, *ACS Appl. Mater. Interfaces*, 2017, **9**, 7160.
10. Y. H. Ding, J. Peng, S. U. Khan and Y. Yuan, *Chem. Eur. J.*, DOI: 10.1002/chem.201700773.
 11. H. X. Yang, T. Song, L. Liu, A. Devadoss, F. Xia, H. Han, H. Park, W. Sigmund, K. Kwon and U. Paik, *J Phys. Chem. C*, 2013, **117**, 17376.
 12. P. Zhu, N. Sheng, M. Li, J. Li, G. Liu, X. Yang, J. Sha, M. Zhu and J. Jiang, *J. Mater. Chem. A*, 2017, DOI: 10.1039/C7TA05254E.
 13. X. H. Xiang, X. C. Li, K. Y. Chen, Y. Tang, M. Wan, X. L. Ding, L. H. Xue, W. X. Zhang and Y. H. Huang, *J. Mater. Chem. A*, 2016, **4**, 18084.
 14. J. Q. Sha, M. T. Li, X. Y. Yang, N. Sheng, J. S. Li, M. L. Zhu, G. D. Liu and J. Z. Jiang, *Cryst. Growth Des.*, 2017, **17**, 3775.